Partial Differential Equations and Applications (2025) 6:34
https://doi.org/10.1007/s42985-025-00340-3

ORIGINAL PAPER

Speckle noise removal in color images using a generalized nonstandard fourth-order variational method

Badreddine Rjaibi[1] · **Didier Auroux**[2]

Received: 20 June 2023 / Accepted: 10 June 2025

Abstract
In this work, we propose a generalized nonstandard fourth-order variational model to remove speckle noise in color images. This method is based on finding the minimum of the q(.) and p(.)-Kirchhoff energy in a specified Banach space. First, we study the existence and uniqueness of the solution for the q(.)-biharmonic and p(.)-Laplacian Euler equations associated with the proposed energy. Then, we consider a fully-discrete forward Euler–Galerkin semi-implicit scheme to find the numerical solution and we study its convergence towards the continuous solution. In the resolution algorithm, the variable exponent functions p(.) and q(.) are chosen adaptively, based on the Di Zenzo gradient and p(.)-Laplacian operator of the image in order to preserve edges and thin structures. Finally, we illustrate the efficiency of our approach with several numerical results.

Keywords Speckle noise removal · Kirchhoff energy · Di Zenzo gradient · Biharmonic operator

Mathematics Subject Classification 35Gxx · 49Mxx · 68U10

1 Introduction

Color image restoration is a challenging task in image processing and particularly in medical imaging field like ultrasound and tomographic images. Various mathematical models are proposed to handle this kind of problem. In these models, the restoration problem with the type of noise that degraded the color image (additive, multiplicative) are modeled with different mathematical tools. PDE-type approaches were suggested for this problem in the case of additive noise (see [1–8]), nevertheless, the multiplicative noise model has not been

This article is part of the section "Applications of PDEs" edited by Seung Yeal Ha.

✉ Badreddine Rjaibi
badreddine.rjaibi@enit.utm.tn

Didier Auroux
didier.auroux@univ-cotedazur.fr

[1] Modélisation Mathématique et Numérique dans les Sciences de l'Ingénieur, LAMSIN, LR99ES20, Université de Tunis El Manar, Ecole Nationale d'Ingénieurs de Tunis, B.P. 37, 1002 Tunis, Tunisia

[2] Laboratoire Jean Alexandre Dieudonné, CNRS, Université Côte d'Azur, Parc Valrose, 06108 Nice Cedex 2, France

Published online: 24 July 2025

studied with this kind of approaches. In this work, we focus on removing multiplicative noise in color images, and in particular the speckle noise [9–11]. The reason is that the majority of data used in the reconstruction of tomographic and ultrasound images is corrupted with speckle noise, which influences the quality of reconstructed images and makes valuable geometric structures (like edges and thin structures) hard to detect.

In [12], the authors report various ways to represent a color image, we consider in this work a RGB (red-green-blue) representation, in which a color image is represented by a vector in three dimensions: $u : \Omega \subset \mathbb{R}^2 \to \mathbb{R}^3$, $(x_1, x_2) \to (u_R, u_G, u_B)$, where (u_R, u_G, u_B) represent the intensity of the three color channels and Ω is an open subset in $\mathbb{R}^2$. We aim at removing the speckle noise in the following degraded image: $f : \Omega \subset \mathbb{R}^2 \to \mathbb{R}^3$, $(x_1, x_2) \to (f_R, f_G, f_B)$, where $f_i = u_i + \eta\sqrt{u_i}$, $i = R, G, B$ and $\eta : \Omega \to \mathbb{R}_+$ is a positive function called the Rayleigh distribution. Our challenge here is then to reconstruct the unnoisy color image u from the noisy color image f.

Some non linear filtering algorithms have been proposed for noise removal in color images, such as the median filter and its extensions [13–17]. The main drawback of this algorithm comes from its mode of application: it is independently applied to each color component. In each color channel, the noisy pixels are supposed to be isolated points and they are replaced by the median value of their nearby pixels' intensities. This allows large intensity modifications of non noisy pixels. This mode of application in the separate color channels leads to a high smoothing in the homogeneous regions, and it cannot guarantee a good preservation of the geometric structures.

The main challenge for removing speckle noise in color images is: how to choose an efficient model that can couple the restoration process between the three color channels, and control the diffusion process in the different parts of the noisy image without losing important geometric structures. The models introduced in [18–20] for removing additive noise are not applicable for this kind of noise. Motivated by [21], we propose to generalize the speckle noise removal in gray level images, using nonstandard fourth-order variational models, to color images as follows. We consider the minimization of the following cost (or energy) function:

$$\min_{u\in X, u_k>0} \left\{ J(u) := \sum_{k=1}^{3} \int_\Omega \frac{\alpha}{q(x)} |\Delta u_k|^{q(x)} + \int_\Omega \frac{\beta}{p(x)} |\nabla u_k|^{p(x)} + \int_\Omega \left(\frac{f_k - u_k}{\sqrt{u_k}} \right)^2 \right\},$$

where $q(x)$ and $p(x) \in [1, 2]$ are the variable exponent functions, α, β are adjustment parameters and X is an appropriate space.

In the proposed energy the superposition between first and second parts is called regularisation term, the third one is the data fitting term. By assuming that $f_k \in L^\infty(\Omega)$ and $inf(f_k) > 0$, we show the proposed energy admits a unique solution $u = (u_1, u_2, u_3)$ in an adequate Banach space, which verifies $inf(f_k) \le u_k \le sup(f_k)$ and u_k is the solution of the following corresponding nonstandard PDE problem :

$$\begin{cases} \Delta^2_{\alpha,q(x)} u_k - \Delta_{\beta,p(x)} u_k + \dfrac{u_k^2 - f_k^2}{u_k^2} = 0 & \text{in } \Omega, \\ \dfrac{\partial(|\Delta u_k|^{q(x)-2}\Delta u_k)}{\partial n} = (|\nabla u_k|^{p(x)-2}\nabla u_k).n = 0 & \text{on } \partial\Omega, \end{cases}$$

for $k = 1, 2, 3$, where $\Delta^2_{\alpha,q(.)} = \Delta(\alpha|\Delta.|^{q(x)-2}\Delta.)$ and $\Delta_{\beta,p(.)} = div(\beta|\nabla.|^{p(x)-2}\nabla.)$ are called the q(.)-biharmonic and p(.)-Laplacian operators (see [21, 22]).

The smoothness degree of the operators $\Delta^2_{\alpha,q(.)}$ and $\Delta_{\beta,p(.)}$ depends on the way the exponents p and q are defined. In order to couple the three color channels and obtain a relaxed smoothness in the homogeneous regions with preservation of the main geometric

structures (such as edges and thin structures), we define the exponents p and q with the Di Zenzo gradient, which is a multichannel color gradient [8], and the p(.)-Laplacian operator. The Di Zenzo gradient is one of the best coupled multichannel color gradient for edge detection. This color gradient is studied in [20] in the additive noise case, and it gave very satisfactory results for the detection of main edges, especially when there is a high level of noise. Some recent works in [21, 23, 24] have proved the interest of second (or higher) order differential operators to detect thin structures.

Inspired by these works, we propose the p(.)-Laplacian to identify filaments and points, which are supposed to be thin structures. In our model, we make an adaptive choice for $p(.)$ and $q(.)$. After the identification of the edges and thin structures using the Di Zenzo gradient and the p(.)-Laplacian operator, we consider the exponent $p(.)$ (respectively $q(.)$) as a function of the standard norm of the Di Zenzo gradient (respectively the p(.)-Laplacian vector) so that $p(.)$ and $q(.) \in [1, 2]$, homogeneous regions are smoothed, and thin structures are preserved in the restoration process.

This paper is organized as follows. Section 2 is devoted to the mathematical study of the proposed model. First, we remind some definitions and generalized Sobolev spaces with variable exponents. Next, we prove the existence and uniqueness of the minimum of the proposed energy. Then, we propose a fully-discrete forward Euler–Galerkin semi-implicit scheme to find the numerical solution and we study its convergence towards the continuous solution of the corresponding nonstandard PDE problem. The algorithm of resolution and its detailed steps are presented in Sect. 3. In Sect. 4, we present the results of several numerical tests in order to study the efficiency of our approach. Finally, some conclusions are given in Sect. 5.

2 Mathematical study of the proposed model

In order to remove speckle noise in color images, we propose to solve the following problem:

$$\min_{u \in X, u_k > 0} \left\{ J(u) := \sum_{k=1}^{3} J_k(u_k) \right\}, \tag{1}$$

where

- $J_k(u_k) := \int_\Omega \frac{\alpha}{q(x)} |\Delta u_k|^{q(x)} + \int_\Omega \frac{\beta}{p(x)} |\nabla u_k|^{p(x)} + \int_\Omega \left(\frac{f_k - u_k}{\sqrt{u_k}} \right)^2$,
- Ω is an open bounded subset of $\mathbb{R}^2$,
- $f = (f_1, f_2, f_3)$ is the noisy color image (with speckle noise), we assume that $f_k \in L^\infty(\Omega)$ and $inf(f_k) > 0$,
- $u = (u_1, u_2, u_3)$ is the restored color image,
- $X = \bigotimes_{k=1}^{3} X_{p,q}^k$, where $X_{p,q}^k = \left\{ u_k \in W^{2,q(.)}(\Omega) \cap W^{1,p(.)}(\Omega) \text{ such that } \frac{\partial u_k}{\partial n} = 0 \right\}$,
- $q(x)$ and $p(x) \in [1, 2]$ are the variable exponent functions,
- α and β are adjustment parameters.

Before moving to the resolution of problem (1), let first remind some definitions and properties of the following spaces: $L^{q(x)}(\Omega)$, $L^{p(x)}(\Omega)$, $W^{1,p(.)}(\Omega)$ and $W^{2,q(.)}(\Omega)$ (for more details, see [22, 25, 26]).

For a given function $r(.) \in C(\overline{\Omega})$, which satisfies the following condition:

$$1 \leq r^- = \min_{x \in \overline{\Omega}} r(x) \leq r(x) \leq r^+ = \max_{x \in \overline{\Omega}} r(x) \leq 2, \tag{2}$$

we define the following space :

$$L^{r(x)} = \left\{ \text{real measurable functions } v : \int_\Omega |v(x)|^{r(x)} dx < +\infty \right\}.$$

Here $L^{r(x)}$ is called the variable exponent generalized Lebesgue space and is equipped with the following norm:

$$\|v\|_{L^{r(.)}} = \inf \left\{ \mu > 0 : \int_\Omega \left| \frac{v(x)}{\mu} \right|^{r(x)} dx \leq 1 \right\}.$$

In the same way, we define the generalized Sobolev spaces as follows:

$$W^{k,r(.)}(\Omega) = \left\{ v \in L^{r(.)} : D^\alpha v \in L^{r(.)} \text{ with } |\alpha| \leq k \right\},$$

where $D^\alpha v = \dfrac{\partial^{|\alpha|} v}{\partial^{\alpha_1} x \partial^{\alpha_2} y}$, with $|\alpha| = \alpha_1 + \alpha_2$ and $k \in \mathbb{N}$.
$W^{k,r(.)}(\Omega)$ is a reflexive and separable Banach space equipped with the following norm:

$$\|v\|_{W^{k,r(.)}} = \sum_{|\alpha| \leq k} \left\| D^\alpha v \right\|_{L^{r(.)}}.$$

In particular, we will use the Banach space $Y = W^{2,q(.)}(\Omega) \cap W^{1,p(.)}(\Omega)$ for solving problem (1), equipped with the norm:

$$\|v\|_Y = \|v\|_{W^{2,q(.)}} + \|v\|_{W^{1,p(.)}}.$$

Proposition 1 *Let $j(x), r(x) \in C(\overline{\Omega})$ satisfying (2).*

- *We have the following continuous embedding :*

$$L^{j(x)} \hookrightarrow L^{r(x)}, \text{ if } j(x) \leq r(x).$$

- *We have*

$$\left(\|Kv\|_{L^{r(.)}}\right)^{r^-} \leq \int_\Omega \frac{1}{r(x)} |Kv|^{r(x)} dx \leq \left(\|Kv\|_{L^{r(.)}}\right)^{r^+}, \text{ if } \|Kv\|_{L^{r(.)}} \geq 1,$$

$$\left(\|Kv\|_{L^{r(.)}}\right)^{r^+} \leq \int_\Omega \frac{1}{r(x)} |Kv|^{r(x)} dx \leq \left(\|Kv\|_{L^{r(.)}}\right)^{r^-}, \text{ if } \|Kv\|_{L^{r(.)}} \leq 1,$$

where K is a linear operator, typically the identity, ∇ or Δ.

The rest of this section is devoted to the development of the theoretical resolution of problem (1).

Lemma 1 *Problem (1) admits a unique solution $u = (u_1, u_2, u_3)$ in X, and it satisfies:*

$$inf\,(f_k) \leq u_k \leq sup\,(f_k), \forall k = 1, 2, 3.$$

Proof Let $(u_k^n) \subset X^k$ be a minimizing sequence of J_k, where $X^k = \{v \in X_{p,q}^k \text{ such that } v > 0\}$. First, let us show that we can assume $inf(f_k) \leq (u_k^n) \leq sup(f_k)$.

Let $K = \{x \in \Omega \text{ such that } u_k^n(x) \leq inf(f_k)\}$ and $v_k^n = max(u_k^n, inf(f_k))$. Then we have:

$$J_k(u_k^n) - J_k(v_k^n) = \int_K \frac{\alpha}{q(x)} |\Delta u_k^n|^{q(x)} + \int_K \frac{\beta}{p(x)} |\nabla u_k^n|^{p(x)} \Big) + \int_K w(u_k^n) - w(inf(f_k)),$$

where $w(u) = \left(\frac{f_k - u}{\sqrt{u}}\right)^2$.

The function w is strictly convex, because $w''(u) = 2\frac{f_k}{u^3} > 0,\ \forall u \in X^k$, and then we have:

$$w\left(u_k^n\right) - w\left(inf(f_k)\right) \geq Dw_u\left(inf(f_k)\right)\left(u_k^n - inf(f_k)\right),$$

where $Dw_u(inf(f_k)) = \frac{(inf(f_k))^2 - (f_k)^2}{(inf(f_k))^2} \leq 0$. So we deduce that $w(u_k^{i+1}) - w(inf(f_k)) \geq 0$ on K. And then that $J_k(u_k^n) - J_k(v_k^n) \geq 0$, so that we can assume that:

$$u_k^n \geq inf\left(f_k\right), \forall n \in \mathbb{N}.$$

The proof of the other half of the property can be achieved in a similar way.

Then, we can easily show that $\|u_k^n\|_{L^{q(x)}}$ and $\|u_k^n\|_{L^{p(x)}}$ are uniformly bounded. Moreover, $J_k^{q,p}(u_k^n) = \int_\Omega \frac{\alpha}{q(x)}|\Delta u_k^n|^{q(x)} + \int_\Omega \frac{\beta}{p(x)}|\nabla u_k^n|^{p(x)}$ is uniformly bounded ((u_k^n) is a minimizing sequence). So we deduce that u_k^n is uniformly bounded in $X_{p,q}^k$, which implies the existence of a subsequence $u_k^{\phi(n)}$ that weakly converges to u_k in $X_{p,q}^k$, and u_k satisfies:

$$inf\left(f_k\right) \leq u_k \leq sup\left(f_k\right), \forall k = 1, 2, 3.$$

Then we deduce $u_k \in Y^k = \{v \in X_{p,q}^k$ such that: $inf(f_k) \leq v \leq sup(f_k)\}$.
Finally, using the fact that J is strictly convex and weakly lower semi continuous in the set Y^k, we deduce the uniqueness of the minimum u_k in Y^k. □

As u_k is the argmin of J_k in Y^k, then we have:

$$0 \in \partial J_k^{p,q}\left(u_k\right) + \frac{u_k^2 - f_k^2}{u_k^2},$$

where $\partial J_k^{p,q}$ is the subdifferential form of $J_k^{p,q}$.

In order to find u_k, we consider the following Euler–Lagrange equation associated to problem (1) :

$$\begin{cases} \Delta\left(\alpha|\Delta u_k|^{q(x)-2}\Delta u_k\right) - div\left(\beta|\nabla u_k|^{p(x)-2}\nabla u_k\right) + \frac{u_k^2 - f_k^2}{u_k^2} = 0 \ \text{ in } \Omega, \\ \frac{\partial\left(|\Delta u_k|^{q(x)-2}\Delta u_k\right)}{\partial n} = \left(|\nabla u_k|^{p(x)-2}\nabla u_k\right).n = 0 \qquad \text{on } \partial\Omega, \end{cases} \tag{3}$$

for $k = 1, 2, 3$.

The operators $\Delta_{\alpha,q(.)}^2 = \Delta(\alpha|\Delta.|^{q(x)-2}\Delta.)$ and $\Delta_{\beta,p(.)} = div(\beta|\nabla.|^{p(x)-2}\nabla.)$ are called the q(.)-biharmonic and p(.)-Laplacian operators (see [21–23]).

Inspired by the work of the authors in [27, 28], we propose to solve numerically the Eq. (3) by using the fully-discrete forward Euler–Galerkin stepping algorithm [29]. The idea is to introduce an artificial time parameter t and then to solve the following equation:

$$\begin{cases} \frac{\partial u_k}{\partial t} + \Delta_{\alpha,q(x)}^2 u_k - \Delta_{\beta,p(x)} u_k + \frac{u_k^2 - f_k^2}{u_k^2} = 0 & \text{in } \Omega \times [0, T], \\ \frac{\partial\left(|\Delta u_k|^{q(x)-2}\Delta u_k\right)}{\partial n} = \left(|\nabla u_k|^{p(x)-2}\nabla u_k\right).n = 0 & \text{on } \partial\Omega \times [0, T], \\ u_k(., 0) = u_k^0 & \text{in } \Omega, \end{cases} \tag{4}$$

for $k = 1, 2, 3$, some final time $T > 0$.

By considering a uniform partition of the time interval [0,T] as follows: $t_i = i\Delta t$, for $i = 0, ..., m$ where $\Delta t = \frac{T}{m}$ and $m \in \mathbb{N}^*$, we define the discrete solution as: $u_k^i(x) = u_k(x, t_i)$.

Then, the discrete semi-implicit scheme of resolution for an initial condition u_k^0 becomes:

$$\frac{u_k^{i+1} - u_k^i}{\Delta t} = -\Delta^2_{\alpha,q(x)} u_k^{i+1} + \Delta_{\beta,p(x)} u_k^{i+1} - \frac{u_k^{i+1} u_k^i - (f_k)^2}{(u_k^i)^2}, \tag{5}$$

with Neumann boundary conditions:

$$\frac{\partial \left(|\Delta u_k^i|^{q(x)-2} \Delta u_k^i \right)}{\partial n} = \left(|\nabla u_k^i|^{p(x)-2} \nabla u_k^i \right).n = 0 \text{ on } \partial\Omega.$$

Lemma 2 *Let $u_k^i \in Y^k = \{v \in X^k_{p,q}$ such that: $inf(f_k) \le v \le sup(f_k)\}$, then problem (5) has a unique solution $u_k^{i+1} \in Y^k$.*

Proof We consider the following function:

$$\begin{aligned} H(u) &= \int_\Omega \left(1 + \frac{\Delta t}{u_k^i}\right) \frac{u^2}{2} - \int_\Omega \left(\Delta t \frac{f_k^2}{(u_k^i)^2} + u_k^i\right) u \\ &\quad + \Delta t \left(\int_\Omega \frac{\alpha}{q(x)} |\Delta u|^{q(x)} + \int_\Omega \frac{\beta}{p(x)} |\nabla u|^{p(x)} \right), \\ &= G_{k,i}(u) + \Delta t J_k^{q,p}(u), \end{aligned}$$

where $G_{k,i}(u) = \int_\Omega \left(1 + \frac{\Delta t}{u_k^i}\right) \frac{u^2}{2} - \int_\Omega \left(\Delta t \frac{f_k^2}{(u_k^i)^2} + u_k^i\right) u.$

G is strictly convex in Y^k, as we have:

$$< \nabla G(u)h, h >= \int_\Omega g''(u) h^2, \ \forall h \in Y^k,$$

where $g(u) = \left(1 + \frac{\Delta t}{u_k^i}\right) \frac{u^2}{2} - \left(\Delta t \frac{f_k^2}{(u_k^i)^2} + u_k^i\right) u$, and then $g''(u) = 1 + \frac{\Delta t}{u_k^i} > 0, \ \forall u \in Y^k$, hence the result of convexity. $J_k^{q,p}$ is also strictly convex in Y^k. Then, we deduce that H is strictly convex in Y^k and the existence and uniqueness of u_k^{i+1} become straightforward. □

Lemma 3 *$\forall i \in \mathbb{N}$, we have*

$$inf\left(inf\left(f_k\right), inf\left(u_k^0\right)\right) \le u_k^i \le sup\left(sup\left(f_k\right), sup\left(u_k^0\right)\right), \text{ if } \Delta t \text{ is small enough.}$$

Proof We denote by $\alpha^i = inf(inf(f_k), inf(u_k^i))$ and $\beta^i = sup(sup(f_k), sup(u_k^i))$. Let $K = \{x \in \Omega$ such that $u_k^{i+1}(x) \ge \beta^i\}$ and $v_k^i = min(u_k^{i+1}, \beta^i)$, then we have:

$$\begin{aligned} H\left(u_k^{i+1}\right) - H\left(v_k^i\right) &= \int_K z\left(u_k^{i+1}\right) - z\left(\beta^i\right) \\ &\quad + \Delta t \left(\int_K \frac{\alpha}{q(x)} \left|\Delta u_k^{i+1}\right|^{q(x)} + \int_K \frac{\beta}{p(x)} \left|\nabla u_k^{i+1}\right|^{p(x)} \right), \\ &= \int_{K_1} z(u_k^{i+1}) - z(\beta^i) \\ &\quad + \Delta t \left(\int_K \frac{\alpha}{q(x)} \left|\Delta u_k^{i+1}\right|^{q(x)} + \int_K \frac{\beta}{p(x)} |\nabla u_k^{i+1}|^{p(x)} \right), \end{aligned}$$

where $z(u) = \left(1 + \frac{\Delta t}{u_k^i}\right)\frac{u^2}{2} - \left(\Delta t \frac{f_k^2}{(u_k^i)^2} + u_k^i\right)u$ and $K_1 = \{x \in \Omega \text{ such that } u_k^{i+1}(x) > \beta^i\}$.

The function z is increasing if $u \in \left[\frac{\Delta t \frac{f_k^2}{(u_k^i)^2} + u_k^i}{1 + \frac{\Delta t}{u_k^i}}, +\infty\right[$, then we can deduce that for a small enough Δt, z is increasing if $u \in [a, +\infty[$, $\forall a > u_k^i$. Then $z(u_k^{i+1}) - z(\beta^i) \geq 0$ on K_1. Indeed: $u_k^{i+1} > \beta^i$ on K_1, which implies the existence of a sequence (a_n^i) such that $u_k^{i+1} > a_n^i > \beta^i$ and $a_n^i \longrightarrow \beta^i$ when $n \longrightarrow +\infty$. We take for example:

$$a_n^i = \frac{u_k^{i+1} - \beta^i}{2n} + \beta^i, \forall n \in \mathbb{N}^*.$$

Then we deduce that $z(u_k^{i+1}) \geq z(a_n^i)$ on K_1. Using the continuity of z and by taking the limit at $+\infty$, we obtain:

$$z\left(u_k^{i+1}\right) \geq z\left(\beta^i\right) \text{ on } K_1.$$

In conclusion, we deduce that $H(u_k^{i+1}) - H(v_k^i) \geq 0$, so we can assume that :

$$u_k^{i+1} \leq sup\left(sup\left(f_k\right), sup\left(u_k^i\right)\right), \forall i \in \mathbb{N},$$

and we iteratively deduce that:

$$u_k^i \leq sup\left(sup\left(f_k\right), sup\left(u_k^0\right)\right).$$

The proof of the other half of the property is achieved in a similary way. □

Lemma 4 *Let $u_k^0 \in Y^k$, then the sequence of solutions (u_k^i) of problem (5) is strongly convergent in $L^2(\Omega)$, $L^{q(x)}(\Omega)$ and $L^{p(x)}(\Omega)$, if Δt is small enough.*

Proof First, we prove the strong convergence of the sequence (u_k^i) in $L^2(\Omega)$. We have

$$\begin{aligned} H\left(u_k^{i+1}\right) - H\left(u_k^i\right) &= \frac{1}{2}\int_\Omega \left(u_k^{i+1}\right)^2 - 2u_k^{i+1}u_k^i + \left(u_k^i\right)^2 \\ &\quad + \int_\Omega \frac{\Delta t}{2u_k^i}\left(\left(u_k^{i+1}\right)^2 - \left(u_k^i\right)^2\right) + \Delta t \frac{f_k^2}{\left(u_k^i\right)^2}\left(u_k^i - u_k^{i+1}\right) \\ &\quad + \Delta t\left(J_k^{q,p}\left(u_k^{i+1}\right) - J_k^{q,p}\left(u_k^i\right)\right), \\ &= \frac{1}{2}\int_\Omega \left(u_k^{i+1} - u_k^i\right)^2 \\ &\quad + \int_\Omega \left(\frac{\Delta t}{2u_k^i}\left(u_k^{i+1} + u_k^i\right) - \Delta t \frac{f_k^2}{\left(u_k^i\right)^2}\right)\left(u_k^{i+1} - u_k^i\right) \\ &\quad + \Delta t\left(J_k^{q,p}\left(u_k^{i+1}\right) - J_k^{q,p}\left(u_k^i\right)\right). \end{aligned}$$

From Lemma 3, we have $\alpha = inf(inf(f_k), inf(u_k^0)) \leq u_k^i \leq \beta = sup(sup(f_k), sup(u_k^0))$ if Δt is small enough. Then we deduce that:

$$\Delta t \frac{\alpha^2 - \beta^2}{\beta^2} \leq \frac{\Delta t}{2u_k^i}\left(u_k^{i+1} + u_k^i\right) - \Delta t \frac{f_k^2}{\left(u_k^i\right)^2} \leq \Delta t \frac{\beta^2 - \alpha^2}{\alpha^2},$$

which implies

$$H\left(u_k^{i+1}\right) - H\left(u_k^i\right) \geq \frac{1}{2}\int_\Omega \left(u_k^{i+1} - u_k^i\right)^2 + \int_\Omega \Delta t \inf\left(C_1\left(u_k^i - u_k^{i+1}\right), C_2\left(u_k^i - u_k^{i+1}\right)\right) + \Delta t(J_k^{q,p}(u_k^{i+1}) - J_k^{q,p}(u_k^i)),$$

where $C_1 = \dfrac{\alpha^2 - \beta^2}{\beta^2}$ and $C_2 = \dfrac{\beta^2 - \alpha^2}{\alpha^2}$.

As we have $u_k^{i+1} = argmin_{Y^K} H(u)$, then we get:

$$\frac{1}{2}\int_\Omega \left(u_k^{i+1} - u_k^i\right)^2 \leq \int_\Omega \Delta t \inf\left(C_1\left(u_k^{i+1} - u_k^i\right), C_2\left(u_k^{i+1} - u_k^i\right)\right) + \Delta t\left(J_k^{q,p}\left(u_k^i\right) - J_k^{q,p}\left(u_k^{i+1}\right)\right).$$

Then for any $N \in \mathbb{N}^*$, we obtain

$$\begin{aligned}\sum_{i=0}^{N-1} \frac{1}{2}\left\|u_k^{i+1} - u_k^i\right\|_{L^2}^2 &= \textstyle\sum_{i=0}^{N-1} \frac{1}{2}\int_\Omega \left(u_k^{i+1} - u_k^i\right)^2 \\ &\leq \int_\Omega \Delta t \inf\left(C_1\left(u_k^N - u_k^0\right), C_2\left(u_k^N - u_k^0\right)\right) \\ &\quad + \Delta t\left(J_k^{q,p}\left(u_k^0\right) - J_k^{q,p}\left(u_k^N\right)\right) \\ &\leq \int_\Omega \Delta t \inf\left(C_1\left(u_k^N - u_k^0\right), C_2\left(u_k^N - u_k^0\right)\right) \\ &\quad + \Delta t J_k^{q,p}\left(u_k^0\right) \\ &< +\infty.\end{aligned}$$

So we deduce the strong convergence of the sequence (u_k^i) in $L^2(\Omega)$.

For the rest of the proof, the strong convergence of the sequence (u_k^i) in $L^{q(x)}(\Omega)$ and $L^{p(x)}(\Omega)$ derives from the continuous embedding $L^2(\Omega) \hookrightarrow L^{q(x)}(\Omega)$ and $L^2(\Omega) \hookrightarrow L^{p(x)}(\Omega)$. □

Lemma 5 *Let $u_k^0 \in Y^k$, then the sequence of solutions (u_k^i) of problem (5) converges to the solution of problem (3).*

Proof Multiplying equation (5) by u_k^{i+1} and integrating on Ω leads to:

$$\int_\Omega \frac{\left(u_k^{i+1}\right)^2 - u_k^i u_k^{i+1}}{\Delta t} = -J_k^{p,q}\left(u_k^{i+1}\right) - \int_\Omega \frac{u_k^i\left(u_k^{i+1}\right)^2 - f_k^2 u_k^{i+1}}{\left(u_k^i\right)^2},$$

which implies that

$$J_k^{p,q}\left(u_k^{i+1}\right) = -\int_\Omega \frac{\left(u_k^{i+1}\right)^2 - u_k^i u_k^{i+1}}{\Delta t} - \int_\Omega \frac{u_k^i\left(u_k^{i+1}\right)^2 - f_k^2 u_k^{i+1}}{\left(u_k^i\right)^2}.$$

From Lemma 3, $\alpha = inf(inf(f), inf(u_k^0)) \leq u_k^i \leq \beta = sup(sup(f), sup(u_k^0))$ if Δt is small enough. As $u_k^0 \in Y^k$, we have:

$$inf\left(f_k\right) \leq u_k^i \leq sup\left(f_k\right),$$

then we deduce that the sequence $(J_k^{p,q}(u_k^i))$ is bounded. In addition, from Lemma 4, we have the strong convergence of the sequence (u_k^i) in $L^{q(x)}(\Omega)$ and $L^{p(x)}(\Omega)$. Then we deduce that the sequence (u_k^i) is bounded in $X_{p,q}^k$. And then there exists a subsequence $u_k^{\phi(i)}$ that weakly converges to u_k in $X_{p,q}^k$, where u_k satisfies:

$$inf(f_k) \leq u_k \leq sup(f_k),$$

which implies that $u_k \in Y^k$.

As $u_k^{\phi(i)}$ is a solution of Eq. (5), then we have

$$0 \in \frac{u_k^{\phi(i+1)} - u_k^{\phi(i)}}{\Delta t} + \partial J_k^{p,q}\left(u_k^{\phi(i+1)}\right) + \frac{u_k^{\phi(i+1)} u_k^{\phi(i)} - f_k^2}{\left(u_k^{\phi(i)}\right)^2},$$

where $\partial J_k^{p,q}$ is the subdifferential form of $J_k^{p,q}$.

This is equivalent to:

$\forall v \in Y^k$,

$$J_k^{p,q}(v) \geq J_k^{p,q}\left(u_k^{\phi(i+1)}\right) + \int_\Omega \left(v - u_k^{\phi(i+1)}\right)\left(\frac{u_k^{\phi(i+1)} - u_k^{\phi(i)}}{\Delta t} + \frac{u_k^{\phi(i+1)} u_k^{\phi(i)} - f_k^2}{\left(u_k^{\phi(i)}\right)^2}\right),$$

which implies that

$\forall v \in Y^k$,

$$J_k^{p,q}(v) \geq \underline{\lim}\, J_k^{p,q}\left(u_k^{\phi(i+1)}\right) + \int_\Omega \left(v - u_k^{\phi(i+1)}\right)\left(\frac{u_k^{\phi(i+1)} - u_k^{\phi(i)}}{\Delta t} + \frac{u_k^{\phi(i+1)} u_k^{\phi(i)} - f_k^2}{(u_k^{\phi(i)})^2}\right).$$

Finally, using the fact that $J_k^{p,q}$ is weakly lower semi continuous in the space X^k, and the dominated convergence theorem, we deduce that

$$\forall v \in Y^k,\ J_k^{p,q}(v) \geq J_k^{p,q}(u_k) + \int_\Omega (v - u_k)\left(\frac{u_k^2 - f_k^2}{u_k^2}\right),$$

which implies

$$0 \in \partial J_k^{p,q}(u_k) + \frac{u_k^2 - f_k^2}{u_k^2}.$$

Then u_k is the solution of problem (3). □

3 Proposed algorithm

In this section we first present our algorithm for solving problem (5), giving the description of its steps and in particular, how to choose the variable exponent functions $p(.)$ and $q(.)$. In the second part, we give some classical methods of speckle noise reduction.

3.1 Algorithm of resolution

For given f, α, β, and Δt, the numerical algorithm of resolution of problem (5) is the following:

Algorithm 1 Proposed Algorithm

Initialize : $i = 0$, $u^0 = (u_1^0, u_2^0, u_3^0)$, p^0 **and** q^0
For i **=0 to N (iterations) do**

1. **For** $k = 1$ **to** 3 **do**
   Compute the solution u_k^{i+1} **of equation (5)**
   End for
2. **Compute the relative error:**

$$Error_{i+1} = \max_{k=1,2,3} \left\{ \frac{\|u_k^i - u_k^{i+1}\|}{\|u_k^i\|} \right\}$$

   If $Error_{i+1} < \epsilon_2$**, break.**
3. **Compute** p^{i+1} **and** q^{i+1}**:**

$$p^{i+1} = 1 + \exp(-k_1 \|\nabla u^{i+1}\|_{DZ})$$

$$q^{i+1} = 1 + \exp\left(-k_2 \sqrt{\sum_{k=1}^{3} (\Delta_p u_k^{i+1})^2}\right)$$

End for

where

- $u = (u_1, u_2, u_3)$ is the original color image,
- k_1, k_2 are positive constants,
- $\|.\|$ is one of the standard norms in $\mathbb{R}^2$,
- $\|\nabla u^{i+1}\|_{DZ}$ is the Di Zenzo gradient norm (see [8, 20, 30]).

The stopping criterion in this algorithm is given by step 2: the algorithm is stopped after N iterations when the relative difference between consecutive iterates $Error_{N+1}$ is smaller than a (small) positive threshold ϵ_2.

In step 1, we compute the solution of Eq. (5) as follows:

$$u_k^{i+1} = \frac{u_k^i}{u_k^i + \Delta t} \left(u_k^i - \alpha \Delta t F_\epsilon^1 \left(u_k^i\right) + \beta \Delta t F_\epsilon^2 \left(u_k^i\right) + \Delta t \frac{f_k^2}{(u_k^i)^2} \right) \tag{6}$$

where

$$F_\epsilon^1 \left(u_k^i\right) = \Delta \left(\left(|\Delta u_k^i| + \epsilon \right)^{q(x)-2} \Delta u_k^i \right),$$

$$F_\epsilon^2 \left(u_k^i\right) = div \left(\left(|\nabla u_k^i| + \epsilon \right)^{p(x)-2} \nabla u_k^i \right),$$

ϵ being a small positive regularisation constant.

In this algorithm, there are two particular cases:

- First case: $p = q = 2$ leads to the so-called biharmonic model.
  We compute u_k^{i+1} using Eq. (6) with $F_\epsilon^1(u_k^i) = \Delta(\Delta u_k^i)$, and $F_\epsilon^2(u_k^i) = \Delta u_k^i$. It is not surprising to obtain modest results with this model, as its isotropic diffusion gives a blurred restored image. This justifies the fact that the diffusion should be relaxed between the homogeneous parts and the geometric structures of the image.

- Second case: $p = q = 1$ leads to the so-called second order TV model.
  We compute u_k^{i+1} using Eq. (6) with $F_\epsilon^1(u_k^i) = \Delta\left((|\Delta u_k^i| + \epsilon)^{-1}\Delta u_k^i\right)$, and $F_\epsilon^2(u_k^i) = div\left((|\nabla u_k^i| + \epsilon)^{-1}\nabla u_k^i\right)$. Note that this model is the slowest one (particularly when ϵ is too small)

Step 3 is the most important part in this algorithm. In order to relax the process of restoration between homogeneous parts and important geometric structures in the image, we adaptively set the indicators p and q based on the Di Zenzo gradient and the p(.)-Laplacian operator as follows:

$$p^{i+1} = 1 + \exp(-k_1\|\nabla u^{i+1}\|_{DZ}) \text{ and } q^{i+1} = 1 + \exp\left(-k_2\sqrt{\sum_{k=1}^{3}(\Delta_p u_k^{i+1})^2}\right).$$

Remarks:

- The Di Zenzo gradient is currently one of the best edge detector for color images. Its particularity is that it not only gives an accurate edge detection, but it is also easy to compute. The multichannel gradient operator is defined in [8] by the square root of the largest eigenvalue of the following tensor matrix:

$$T = \begin{pmatrix} T_{11} & T_{12} \\ T_{12} & T_{22} \end{pmatrix},$$

where $T_{lm} = \sum_{k=1}^{3} \frac{\partial u_k^{i+1}}{\partial x_l}\frac{\partial u_k^{i+1}}{\partial x_m}$, $1 \le l, m \le 2$, and the norm of this gradient is given by:

$$\left\|\nabla u^{i+1}\right\|_{DZ}^2 = \frac{1}{2}\left[T_{11} + T_{22} + \sqrt{(T_{11} - T_{22})^2 + 4T_{12}^2}\right]. \tag{7}$$

In [20], the authors give a simplified equivalent formulation as follows:

$$\left\|\nabla u^{i+1}\right\|_{DZ}^2 = F(\nabla u^{i+1})\sum_{k=1}^{3}\left|\nabla u_k^{i+1}\right|^2 \tag{8}$$

where the function F is defined by:

$$F(\nabla u^{i+1}) = \begin{cases} \dfrac{1 + \sqrt{1 - 4g(\nabla u^{i+1})}}{2} \text{ if } \nabla u^{i+1} \neq 0, \\ 1 \text{ if } \nabla u^{i+1} = 0, \end{cases}$$

with

$$g(\nabla u) = \frac{det^2(\nabla u_1^{i+1}, \nabla u_2^{i+1}) + det^2(\nabla u_1^{i+1}, \nabla u_3^{i+1}) + det^2(\nabla u_2^{i+1}, \nabla u_3^{i+1})}{\left(\left|\nabla u_1^{i+1}\right|^2 + \left|\nabla u_2^{i+1}\right|^2 + \left|\nabla u_3^{i+1}\right|^2\right)^2} \tag{9}$$

with

$$det^2(\nabla u_r^{i+1}, \nabla u_s^{i+1}) = \left(\frac{\partial u_r^{i+1}}{\partial x_1}\frac{\partial u_s^{i+1}}{\partial x_2} - \frac{\partial u_r^{i+1}}{\partial x_2}\frac{\partial u_s^{i+1}}{\partial x_1}\right)^2, \text{ for } r, s = 1, 2, 3,$$

and $|.|$ is the Frobenius norm in $\mathbb{R}^2$.

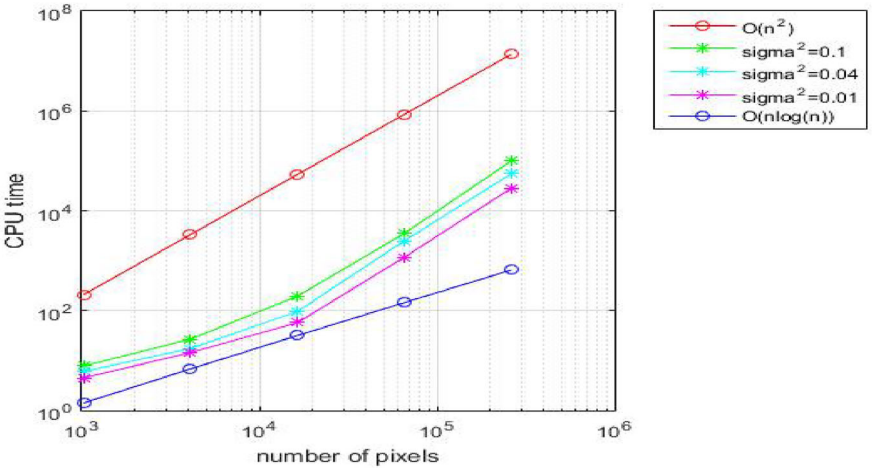

Fig. 1 Evolution in logarithmic scale of the CPU time as a function of the number of pixels for different noise levels with $\epsilon_2 = 10^{-4}$

- Inspired from the previous works in [21, 23, 24, 31, 32], we choose the p(.)-Laplacian operator to detect thin structures in the color image. However, first order differential operators (such as the classical gradient) cannot see thin structures [24]. Filaments and points in the image are usually considered as thin structures, as there is no modification of the intensity across the jump, which is not the case for edges. In the presence of noise, the detection of such small irregular objects becomes more difficult. For the above reason, we need to use a higher order differential operator, as the p(.)-Laplacian, to enhance the detection of thin structures.
- In the smoothest parts of the image, the Di Zenzo gradient and the multichannel p-Laplacian have small norm values, close to zero, thus p^{i+1} and q^{i+1} take values close to 2, and the restoration process becomes then isotropic in these regions. Nearby the geometric thin structures of the image, the following norms $\|\nabla u^{i+1}\|_{DZ}$ and $\sqrt{\sum_{k=1}^{3}(\Delta_p u_k^{i+1})^2}$ have much larger values, thus p^{i+1} and q^{i+1} will take values close to 1 and the diffusion becomes relaxed and anisotropic.
- The complexity of this algorithm is based on three key factors: the size of the image, the noise level and the stopping criterion threshold. We mention that the complexity of the biharmonic model and the second-order TV model, applied to grayscale problems, is respectively $O(n\log(n))$ and $O(n^2)$, where n is the number of pixels in the image (see [2, 20, 28]). As our algorithm diffuses in a relaxed manner between homogeneous areas and geometric structures of the image, we can expect a complexity of at best $O(n\log(n))$ and at worst $O(n^2)$. We performed the numerical simulation using Matlab 8.5 (R2015a) by running the program on a desktop computer with an Intel Core i5, 4.6 GHz CPU and 8 GB of RAM.
  Figure 1 illustrates the complexity behavior of our algorithm with respect to $O(n^2)$ and $O(nlog(n))$ for different noise levels, with $\epsilon 2 = 10^{-4}$.

3.2 Some classical methods of speckle noise reduction

- **Median Filter [33] :** The median filter is a nonlinear method where each pixel is replaced by the median value of its 3×3 neighboring pixels.
- **Kuan Filter [34]:** The Kuan filter approach transforms the speckle noise model into an additive linear resolution form as shown in the following equation :

$$I_F = I.W + \overline{I}.(1 - W),$$

where :

  - I is the observed image (corrupted with speckle noise),
  - I_F is the filtered image,
  - $W = \dfrac{1 - \dfrac{c_u^2}{c_i^2}}{1 + c_u^2}$ is the weighting factor,
  - $c_u = \dfrac{\sigma_u}{\overline{u}}$ and $c_i = \dfrac{\sigma_I}{\overline{I}}$
  - $\overline{u}$ is the mean value of the speckle noise image u ,
  - σ_u is the speckle noise variance,
  - $\overline{I}$ is the mean value of I,
  - σ_I is the variance of I.

- **Frost Filter [35]:** Filtering the image with a Frost filter consists in estimating the filtered pixel values as follows:

  - Define a fixed $n \times n$ (n=5 or 3) pixels local window in the noisy image centred at the pixel of interest.
  - Convolve the local window with a weighting factor as follows:

$$y = \frac{\sum x * w}{\sum w},$$

    where:
      * x is the defined local window,
      * $w = \exp(-kc_x|t_0|)$ is the weighting factor,
      * $c_x = \frac{\sigma_x}{\overline{x}}$, where $\overline{x}$ and σ_x are the mean value and the variance of x,
      * $|t_0|$ is the distance between the center pixel and the other pixels in x,
      * k is the damping factor.
  - Replace the value of the pixel of interest with the corresponding filtered pixel value.

- **A variational adaptive method: Second-order TGV model** This model was proposed in [36] to eliminate the additive noise present in MRI images. In order to adapt it to speckle noise suppression, we minimize the following energy:

$$\min_{u_k>0} \left\{ TGV_\alpha^2(u_k) + \int_\Omega \left(\frac{f_k - u_k}{\sqrt{u_k}} \right)^2 d\mu(x) \right\}, \forall k = 1, 2, 3, \tag{10}$$

where

$$TGV_\alpha^2(u_k) = \sup\{ \int_\Omega u_k div^2(w) d\mu(x) \mid w \in C_c^2\left(\Omega, Sym^2\left(\mathbb{R}^2\right)\right), \\ \|div^i(w)\| \leq \alpha_i, i = 0, 1\}.$$

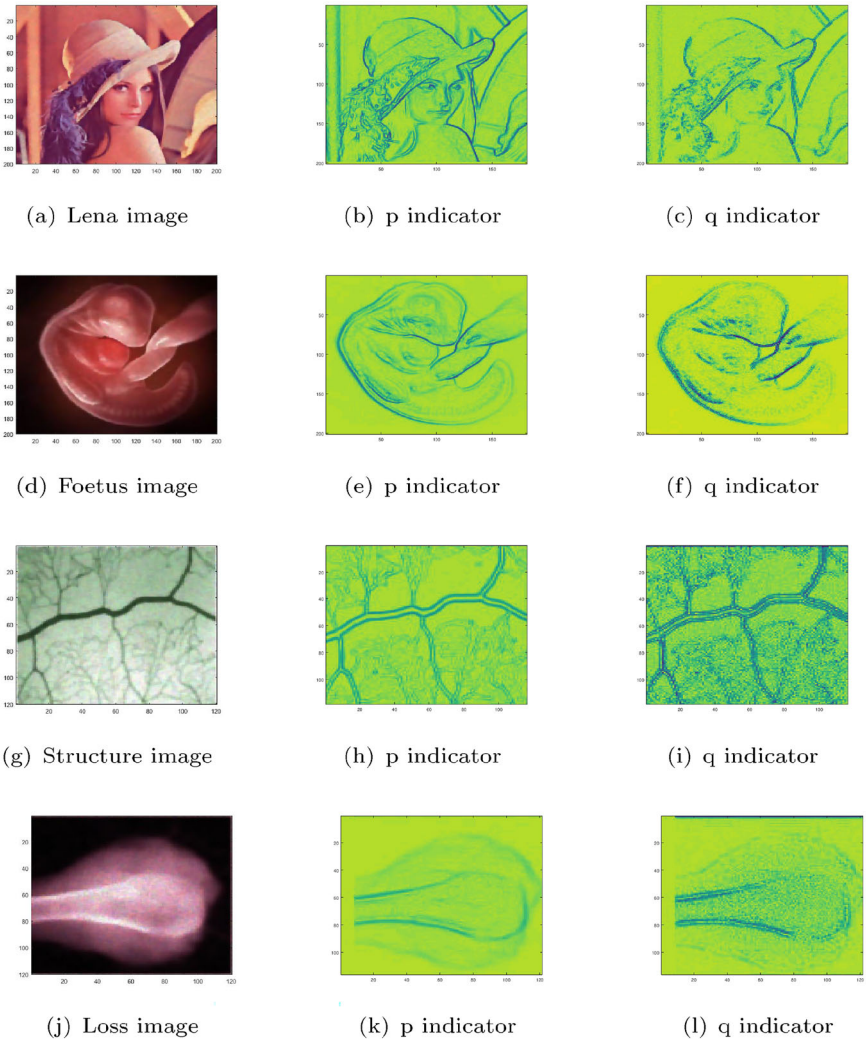

Fig. 2 Example of identified geometric structures on some tested color images

4 Numerical tests

In this section, we present several numerical tests, in order to study the efficiency of our algorithm.

Figure 2 shows some examples of original images and corresponding p and q indicators. The original images are corrupted with a speckle noise for different levels of variance $\sigma^2 \in \{0.01, 0.02, 0.04, 0.1, 0.3\}$. In these tests, in order to quantify the quality of restoration, we choose the SSIM indicator (Structural Similarity), the PSNR (Peak Signal to Noise Ratio), the MSE (relative mean squared error) and the speckle index $\text{SSI} = \frac{\sigma^2}{\overline{I}}$, where $\overline{I}$ is the mean value of the restored image. Restored images that have a SSIM index between 0.7 and 1,

Table 1 Sensitivity of indicators with respect to α with $\sigma^2 = 0.01$, $\beta = 20$ and $\Delta t = 0.01$

Indicator	Structure image				Lena image			
	SSIM	PSNR	MSE	SSI	SSIM	PSNR	MSE	SSI
$\alpha = 0$	0.804	28.38	0.0539	0.0142	0.903	31.06	0.0534	0.0192
$\alpha = 0.01$	0.807	28.54	0.0529	0.0142	0.904	31.14	0.0536	0.0192
$\alpha = 0.1$	**0.827**	**30.54**	**0.042**	**0.0140**	**0.912**	**32**	**0.05**	**0.0190**
$\alpha = 1$	0.810	28.71	0.0510	0.0142	0.902	31.04	0.0533	0.00191
$\alpha = 10$	0.799	28.48	0.0535	0.0142	0.900	31	0.0541	0.0192
$\alpha = 100$	0.753	28.19	0.0563	0.0142	0.848	29.27	0.0696	0.0192
$\alpha = 200$	0.69	26.76	0.0669	0.0143	0.756	26.53	0.1	0.0193
$\alpha = 1000$	0.0376	9.2	16.22	0.0160	0.110	11.49	2.09	0.0210

Optimal values are in bold

Table 2 Sensitivity of indicators with respect to β with $\sigma^2 = 0.01$, $\alpha = 0.1$ and $\Delta t = 0.01$

Indicator	Structure image				Lena image			
	SSIM	PSNR	MSE	SSI	SSIM	PSNR	MSE	SSI
$\beta = 0$	0.594	23.16	0.0989	0.0142	0.756	25.84	0.1	0.0192
$\beta = 0.5$	0.605	23.43	0.0962	0.0142	0.763	26.08	0.0967	0.0192
$\beta = 2$	0.627	23.96	0.0897	0.0142	0.7841	26.81	0.0898	0.00192
$\beta = 10$	0.7266	26.48	0.0668	0.0141	0.8618	29.74	0.0626	0.0191
$\beta = 20$	**0.827**	**30.54**	**0.042**	**0.0140**	**0.912**	**32**	**0.05**	**0.0190**
$\beta = 50$	0.56	25.09	0.0812	0.0142	0.650	23.98	0.13	0.0193
$\beta = 100$	0.237	17	0.216	0.0145	0.361	17.18	0.339	0.0194

Optimal values are in bold

Table 3 Sensitivity of indicators according to Δt with $\sigma^2 = 0.01$, $\alpha = 0.1$ and $\beta = 20$

Indicator	Structure image				Lena image			
	SSIM	PSNR	MSE	SSI	SSIM	PSNR	MSE	SSI
$\Delta t = 0.001$	0.62	23.58	0.0915	0.0142	0.78	26.69	0.0901	0.0194
$\Delta t = 0.01$	**0.827**	**30.54**	**0.042**	**0.0140**	**0.912**	**32**	**0.05**	**0.0190**
$\Delta t = 0.1$	0.151	14.38	0.52	0.0147	0.226	14.23	1.94	0.0197

Optimal values are in bold

PSNR values between 25db and 40db, MSE value close to or smaller than 10^{-2} and a SSI value close to that of the original image are assumed to be of good quality.

The choice of parameters α and β will affect the level of regularization of the images. These parameters keep a balance between denoising and preserving the important objects and edges. k_1 and k_2 are two threshold positive parameters, generally we take them very small to reduce the effect of noise on geometric structures (edges and thin structures).

For all numerical examples presented here, we set $\alpha = 0.1$, $\beta \in \{10, 15, 20\}$, $\Delta t = 0.01$, $k_1 = 0.005$, $k_2 = 0.03$, $p^0 \equiv 2$ and $q^0 \equiv 1$, and the algorithm is stopped when $Error_{N+1}$ is smaller than ϵ_2, with typical values of $\epsilon_2 = 10^{-4}$, 10^{-6}, or 10^{-8}. The choices of the optimal values of the parameters α, β and Δt have been studied on the Lena image example in Tables 1, 2 and 3, in which we study the indicators sensitivity with respect to these parameters for a standard level of noise ($\sigma^2 = 0.01$).

(a) $k2 = 0.001$ (b) $k2 = 0.01$ (c) $k2 = 0.1$

Fig. 3 The map generated by the indicator q of the Lena image with $k1 = 0.005$ and different values of $k2$

(a) $k1 = 0.005$ (b) $k1 = 0.01$ (c) $k1 = 0.1$

Fig. 4 The map generated by the indicator p of the Lena image with $k2 = 0.01$ and different values of $k1$

Based on previous works on the second order variational model to remove speckle noise [21, 23, 28], we take $\beta = 20$, $\Delta t = 0.01$, k_1 of the order of 10^{-3} and k_2 of the order of 10^{-2}. Figure 3 shows the map generated by the indicator q of the Lena image with $k1 = 0.005$ and different values of $k2$, Fig. 4 shows the map generated by the indicator p of the Lena image with $k2 = 0.01$ and different values of $k1$.

Table 1 shows the evolution of the indicators of restoration quality according to the parameter α with $\beta = 20$, $\Delta t = 0.01$ and $\sigma^2 = 0.01$. We can see that the optimal value of α is 0.1, for which the values of the indicators are the best. The obtained values of SSIM, PSNR, MSE and SSI according to β with $\alpha = 0.1$, $\sigma^2 = 0.01$ and $\Delta t = 0.01$ shown in Table 2, confirm our choice of the optimal value of β.

In order to confirm the results of convergence in Lemmas 3 and 4, we present in Table 3 the indicators sensitivity according to three values of Δt with $\sigma^2 = 0.01$, $\alpha = 0.1$ and $\beta = 20$. The optimal value of Δt is 0.01, for which we obtained the best values of SSIM, PSNR, SSI and a relative error (MSE) smaller than 5%. For $\Delta t = 0.001$, the obtained results are modest, the SSIM is smaller than 0.7 and the relative error is between 9% and 10%. These results are not suprising, in fact, if we replace Δt by 0 in the Eq. (6), we obtain $u_k^{i+1} = u_k^i$, $\forall i$ proving the convergence of the sequence (u_k^i) to the initial solution u_k^0. The bad results obtained with $\Delta t = 0.1$ confirm that Δt should be very small to have the convergence of the solutions sequence (u_k^i).

Figures 5a, e and i show the noised color images with a speckle noise variance $\sigma^2 = 0.02$.

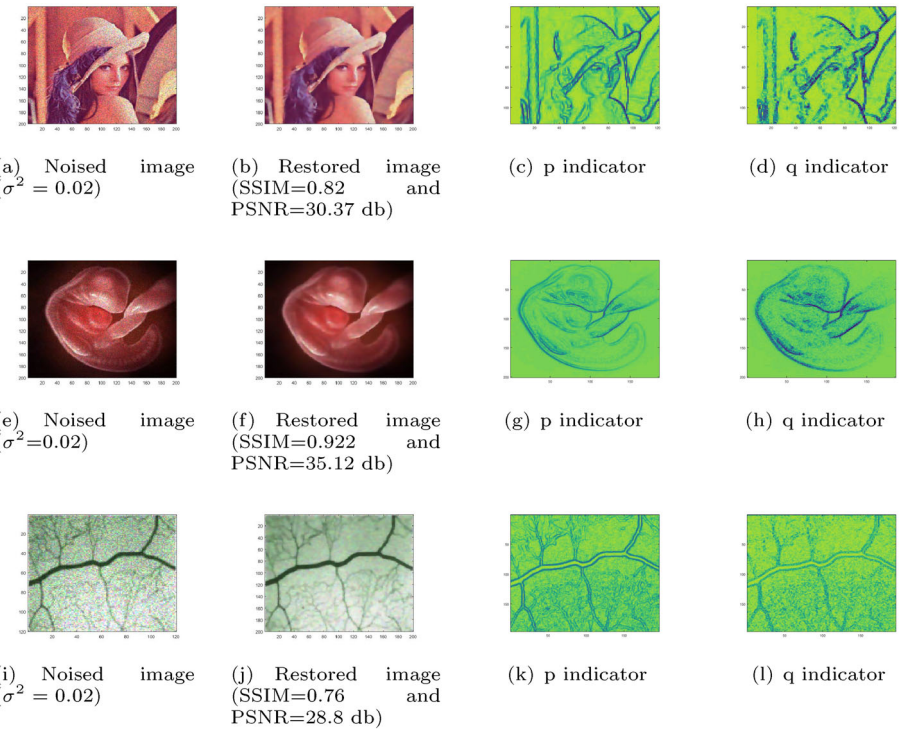

(a) Noised image ($\sigma^2 = 0.02$)
(b) Restored image (SSIM=0.82 and PSNR=30.37 db)
(c) p indicator
(d) q indicator
(e) Noised image (σ^2=0.02)
(f) Restored image (SSIM=0.922 and PSNR=35.12 db)
(g) p indicator
(h) q indicator
(i) Noised image ($\sigma^2 = 0.02$)
(j) Restored image (SSIM=0.76 and PSNR=28.8 db)
(k) p indicator
(l) q indicator

Fig. 5 Restored image with our method from the noised image ($\sigma^2 = 0.02$)

Figures 5b, f, j, 6a, e and i show the restored color images by our approach with their corresponding SSIM and PSNR indicators when $\sigma^2 = 0.02$ and $\sigma^2 = 0.04$.

One can see the efficiency of our approach for this level of noise. This shows that this method is not very sensitive to the presence of high level of noise. The obtained restoration quality indicators are very good for the two levels of noise. The SSIM index are larger than 0.7, PSNR values are between 26db and 38db and the SSI index is close to that of the original image (see Fig. 7d–f).

Figures 5c, g, k, 9c, g, k and o, show the isovalues of the variable exponent p(.) edge indicator in the image.

Figures 5d, h, l, 9d, h, l and p, show the isovalues of the variable exponent q(.) (indicator of thin structures) in the image. p and q describe the different objects in the image. Nearby the geometric structures, i.e. edges and thin structures, the values of p and q are close to 1, while the values of p and q are close to 2 in homogenous regions. We can say that this result highlights the importance of the high-order terms in thin structure detection and preserving.

In order to prove the efficiency of our method, we make a comparison with three standard methods of speckle noise reduction: the median filter, the Kuan filter and the Frost filter. The color images presented in Fig. 2a, d and g, are chosen for comparaison. The indicators of the quality of the restored images, the SSIM, PSNR, SSI and the relative error are given in Tables 4, 5 and 6. The evolution of SSIM and SSI depending on noise level is presented in Fig. 7.

We can see in these tables and on Fig. 7 that the best indicator results are achieved with our approach for the different noise levels. For $\sigma^2 \leq 0.04$, the SSIM indicator is larger than

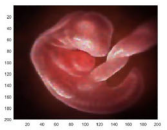

(a) Restored image with our method (SSIM=0.9 and PSNR=33.6 db)

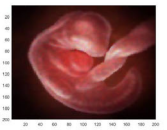

(b) Restored image with Kuan filter (SSIM=0.887 and PSNR=32.55 db)

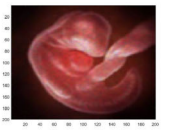

(c) Restored image with Frost filter (SSIM=0.88 and PSNR=32.25 db)

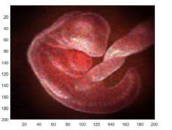

(d) Restored image with median filter (SSIM=0.78 and PSNR=29.9 db)

(e) Restored image with our method (SSIM=0.77 and PSNR=28.03 db)

(f) Restored image with Kuan filter (SSIM=0.73 and PSNR=27.5 db)

(g) Restored image with Frost filter (SSIM=0.72 and PSNR=26.96 db)

(h) Restored image with median filter (SSIM=0.575 and PSNR=24.54 db)

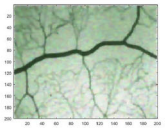

(i) Restored image with our method (SSIM=0.70 and PSNR=26.68 db)

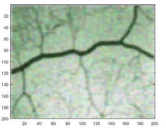

(j) Restored image with Kuan filter (SSIM=0.60 and PSNR=25.57 db

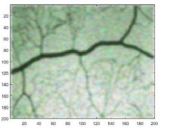

(k) Restored image with Frost filter (SSIM=0.61 and PSNR=25.57 db

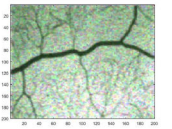

(l) Restored image with median filter (SSIM=0.465 and PSNR=21.66 db

Fig. 6 Comparison of the restored images with some classical methods with $\sigma^2 = 0.04$

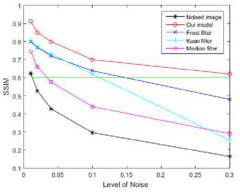

(a) Restored Lena image SSIM values

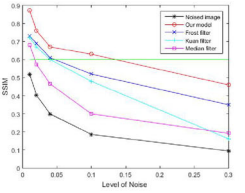

(b) Restored structure image SSIM values

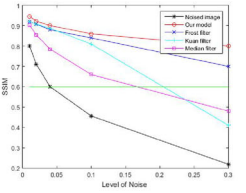

(c) Restored Foetus image SSIM values

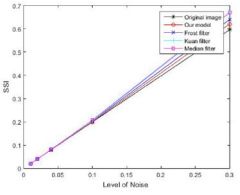

(d) Restored Lena image SSI values

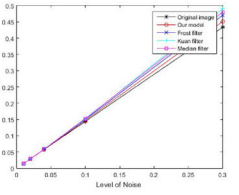

(e) Restored structure image SSI values

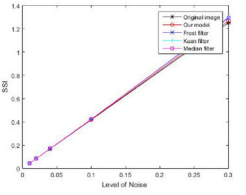

(f) Restored Foetus image SSI values

Fig. 7 Evolution of SSIM and SSI versus noise level

Table 4 Comparison with some classical methods on the Lena image

Level of Noise	$\sigma^2 = 0.01$				$\sigma^2 = 0.02$			
Indicators	SSIM	PSNR	Error	SSI	SSIM	PSNR	Error	SSI
Our proposed model	0.912	32	0.05	0.0199	0.85	30.37	0.060	0.0398
Frost filter	0.798	27.98	0.10	0.0199	0.767	27.64	0.102	0.0399
Kuan filter	0.802	28.47	0.0814	0.0199	0.77	28.21	0.082	0.04
Median filter	0.743	29	0.09	0.02	0.66	26.97	0.148	0.0401
Level of Noise	$\sigma^2 = 0.04$				$\sigma^2 = 0.1$			
Indicators	SSIM	PSNR	Error	SSI	SSIM	PSNR	Error	SSI
Our proposed model	0.80	28.03	0.08	0.0797	0.7	26	0.09	0.2
Frost filter	0.72	26.96	0.106	0.0802	0.638	25	0.11	0.203
Kuan filter	0.73	27.5	0.085	0.0803	0.62	24.8	0.117	0.203
Median filter	0.575	24.54	0.2	0.0805	0.44	21	0.3	0.207

Level of Noise	$\sigma^2 = 0.3$			
Indicators	SSIM	PSNR	Error	SSI
Our proposed model	0.6	22.3	0.13	0.62
Frost filter	0.48	20.57	0.18	0.64
Kuan filter	0.254	16	0.33	0.67
Median filter	0.29	16.88	0.3	0.67

Table 5 Comparison with some classical methods on the structure image

Level of Noise	$\sigma^2 = 0.01$				$\sigma^2 = 0.02$			
Indicators	SSIM	PSNR	Error	SSI	SSIM	PSNR	Error	SSI
Our proposed model	0.827	30.54	0.042	0.0144	0.76	28.8	0.050	0.0289
Frost filter	0.73	26.97	0.0655	0.0145	0.69	26.4	0.0691	0.0290
Kuan filter	0.722	26.59	0.0685	0.0145	0.67	26.09	0.0719	0.0291
Median filter	0.682	25.61	0.109	0.0146	0.574	23.8	0.14	0.0292
Level of Noise	$\sigma^2 = 0.04$				$\sigma^2 = 0.1$			
Indicators	SSIM	PSNR	Error	SSI	SSIM	PSNR	Error	SSI
Our proposed model	0.70	26.68	0.065	0.0580	0.63	24	0.087	0.147
Frost filter	0.61	25.57	0.0754	0.0584	0.52	23	0.098	0.15
Kuan filter	0.60	25.17	0.0789	0.0586	0.48	22	0.1	0.151
Median filter	0.465	21.66	0.192	0.0585	0.3	17	0.2	0.153

Level of Noise	$\sigma^2 = 0.3$			
Indicators	SSIM	PSNR	Error	SSI
Our proposed model	0.46	20	0.15	0.451
Frost filter	0.35	18.6	0.175	0.47
Kuan filter	0.162	14	0.28	0.49
Median filter	0.192	14.3	0.27	0.48

Table 6 Comparison with some classical methods on the Foetus image

Level of Noise	$\sigma^2 = 0.01$				$\sigma^2 = 0.02$			
Indicators	SSIM	PSNR	Error	SSI	SSIM	PSNR	Error	SSI
Our proposed model	0.946	37.11	0.0540	0.0418	0.922	35.12	0.070	0.0837
Frost filter	0.9201	33.34	0.0919	0.0418	0.908	32.96	0.0944	0.0837
Kuan filter	0.9206	33.57	0.0856	0.0418	0.908	33.22	0.0894	0.0838
Median filter	0.903	34.88	0.104	0.0419	0.8542	32.56	0.143	0.0840
Level of Noise	$\sigma^2 = 0.04$				$\sigma^2 = 0.1$			
Indicators	SSIM	PSNR	Error	SSI	SSIM	PSNR	Error	SSI
Our proposed model	0.901	33.6	0.08	0.1676	0.86	31.2	0.09	0.419
Frost filter	0.88	32.25	0.099	0.1678	0.84	30.9	0.108	0.4217
Kuan filter	0.887	32.55	0.093	0.1678	0.81	30	0.118	0.4218
Median filter	0.785	29.9	0.19	0.1682	0.66	26.4	0.299	0.4215

Level of Noise	$\sigma^2 = 0.3$			
Indicators	SSIM	PSNR	Error	SSI
Our proposed model	0.8	29	0.12	1.268
Frost filter	0.7	27	0.15	1.293
Kuan filter	0.41	20.5	0.347	1.3
Median filter	0.48	21.66	0.31	1.295

70%, the relative error is smaller than 8%, the PSNR is the best one and the SSI value is the nearest one to that of the original image.

The results obtained by the Frost filter, Kuan filter and median filter are globally worse, the SSIM indicator is not always larger than 70%, the relative error is not close to 8% in most cases, the SSI value is not the nearest one to that of the original image, only the value of the PSNR is good. It is not surprising to obtain such results with these filters, as they process the image locally in small windows centred at the pixel of interest, leading to artifacts in the restoration process. These results confirm the fact that the restoration diffusion should be relaxed between the homogeneous parts and the geometric structures of the image. We can also see in these tables, that our approach is much less degraded when the level of noise is increased ($\sigma^2 > 0.04$).

For the same images, we show in Fig. 8 a comparison of the extrema between restored images by our approach and the noisy ones for every iteration. We can see that the three channels of the restored image verify the condition of Lemma 1:

$$inf(f_k) \leq u_k^i \leq sup(f_k), \forall k = 1, 2, 3.$$

Still for validating the effectiveness of our approach, we propose to test it on less synthetic and more realistic medical images as shown in Fig. 9.

Figures 10, 11 and Tables 7, 8 highlight that our model provides better image quality compared to the second-order TGV model for the two levels of noise ($\sigma^2 = 0.04$ and $\sigma^2 = 0.1$). The results obtained by the second-order TGV model are generally satisfactory, but the SSIM, PSNR, and SNR values are lower than those produced by our approach for different noise levels. The comparison results are not surprising, given that the second order TGV

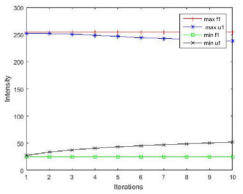

(a) max/min of u1 and f1 (Structure image)

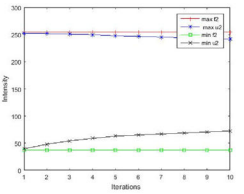

(b) max/min of u2 and f2 (Structure image)

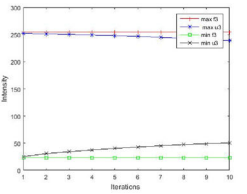

(c) max/min of u3 and f3 (Structure image)

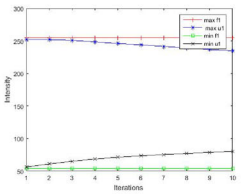

(d) max/min of u1 and f1 (Lena image)

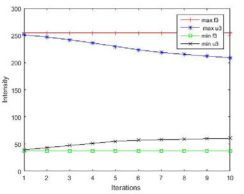

(e) max/min of u2 and f2 (Lena image)

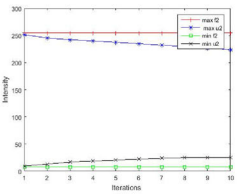

(f) max/min of u3 and f3 (Lena image)

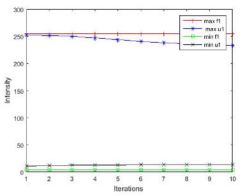

(g) max/min of u1 and f1 (Foetus image)

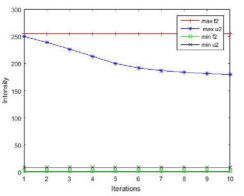

(h) max/min of u2 and f2 (Foetus image)

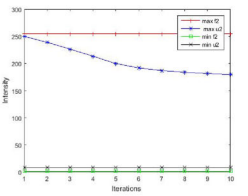

(i) max/min of u3 and f3 (Foetus image)

Fig. 8 The extremum principle with a comparison between restored image and noisy one for every iteration

model removes noise in the image independently for each channel. In contrast, our approach considers the coordination between channels during the restoration process.

Figures 12 and 13 show the results of our approach in the presence of other types of noise that may appear in an image during a clinical examination. Examples include Gaussian noise, Poisson noise and salt and pepper noise. The noise level tested in this experiment is set by default. We see that the elimination of Gaussian noise and Poisson noise was carried out very satisfactorily, as evidenced by the SSIM and PSNR values displayed. However, it is less effective for salt and pepper noise.

Among the important phases in medical imaging, segmentation is a crucial step. It consists of extracting, from the image, one or more regions representative of the area of interest. In our experiment, represented in Fig. 14, we used the watershed method for segmentation (for more details, see [37]). This method is mainly based on good restoration and detection of the geometric structures of the image, which is ensured by our approach.

Figure 14c shows red blood cells segmented as 31 regions, each surrounded by black lines; Fig. 14f shows the tumor area in the brain segmented, a single region surrounded by an orange line; Fig. 14i shows the coronavirus-infected area in the lung segmented, with the region colored in green; Finally, Fig. 14l shows the tumor area in the lung segmented, a single region surrounded by an orange line.

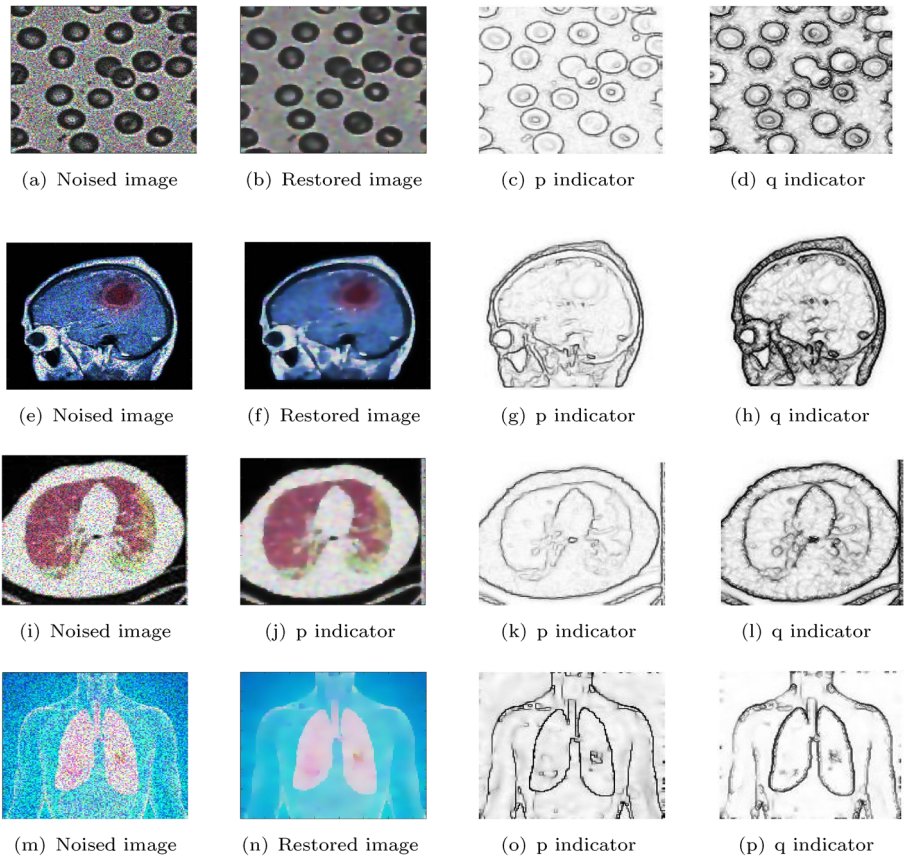

Fig. 9 Some other results obtained with our method from noised medical images where $\sigma^2 = 0.1$

5 Conclusion

In this work, we generalized to color images the non standard $q(.)$-Kirchhoff model for removing speckle noise in gray level images. The proposed model is based on the resolution of the $q(.)$-biharmonic and $p(.)$-Laplacian coupled problem with Neumann boundary conditions, where p and q are adaptively chosen based on the Di Zenzo gradient and the $p(.)$-Laplacian operator of the image.

We studied the semi-implicit scheme used to numerically solve the proposed problem, and we proved the existence and uniqueness of a sequence converging to the exact solution of the original problem in an adequate Banach space.

The numerical experiments we presented here confirm the efficiency of this approach. The obtained numerical results show a very good quality of the restored images, with identification and preservation of important geometric structures.

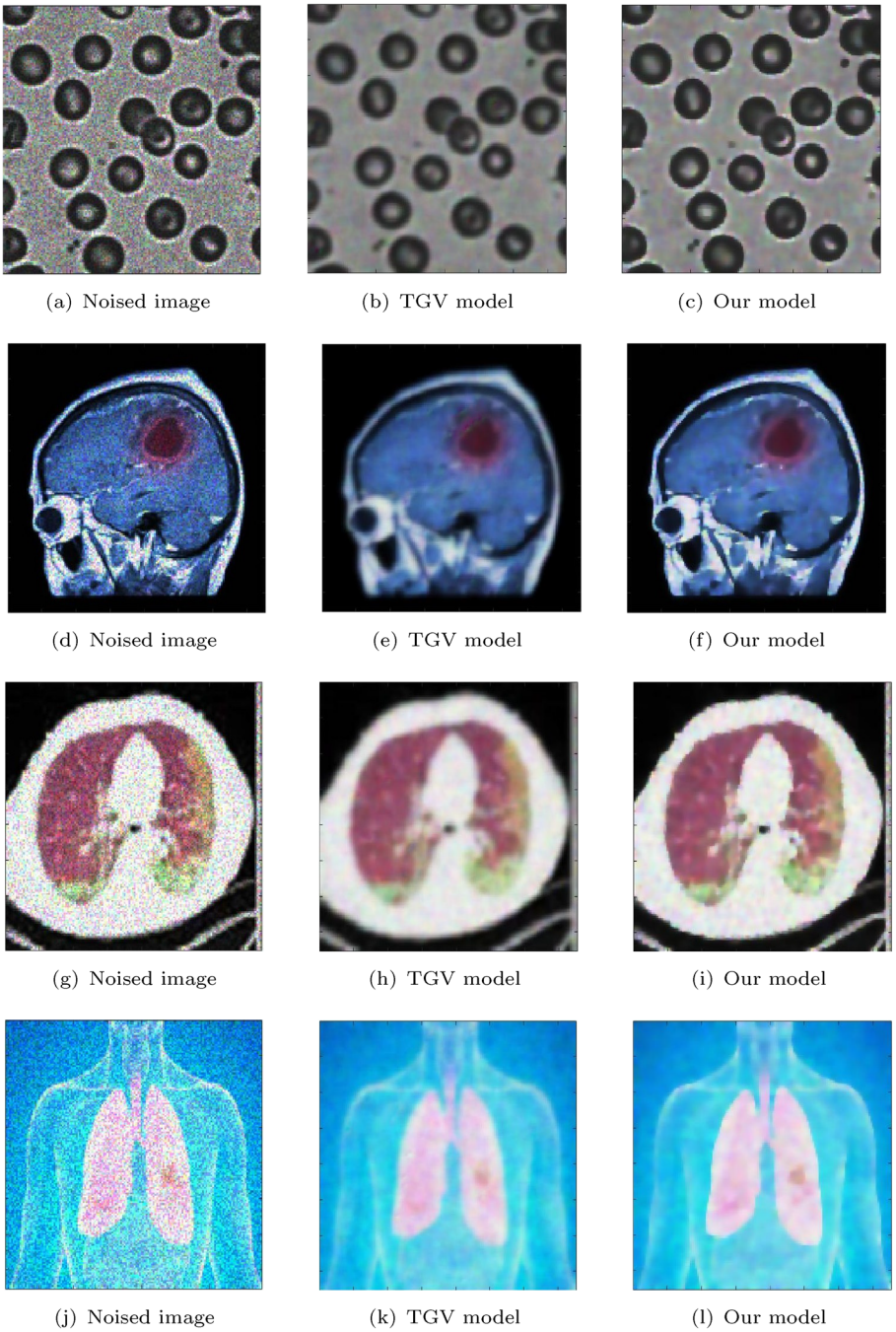

(a) Noised image (b) TGV model (c) Our model

(d) Noised image (e) TGV model (f) Our model

(g) Noised image (h) TGV model (i) Our model

(j) Noised image (k) TGV model (l) Our model

Fig. 10 Comparaison of the restored images obtained by our and TGV model with $\sigma^2 = 0.04$

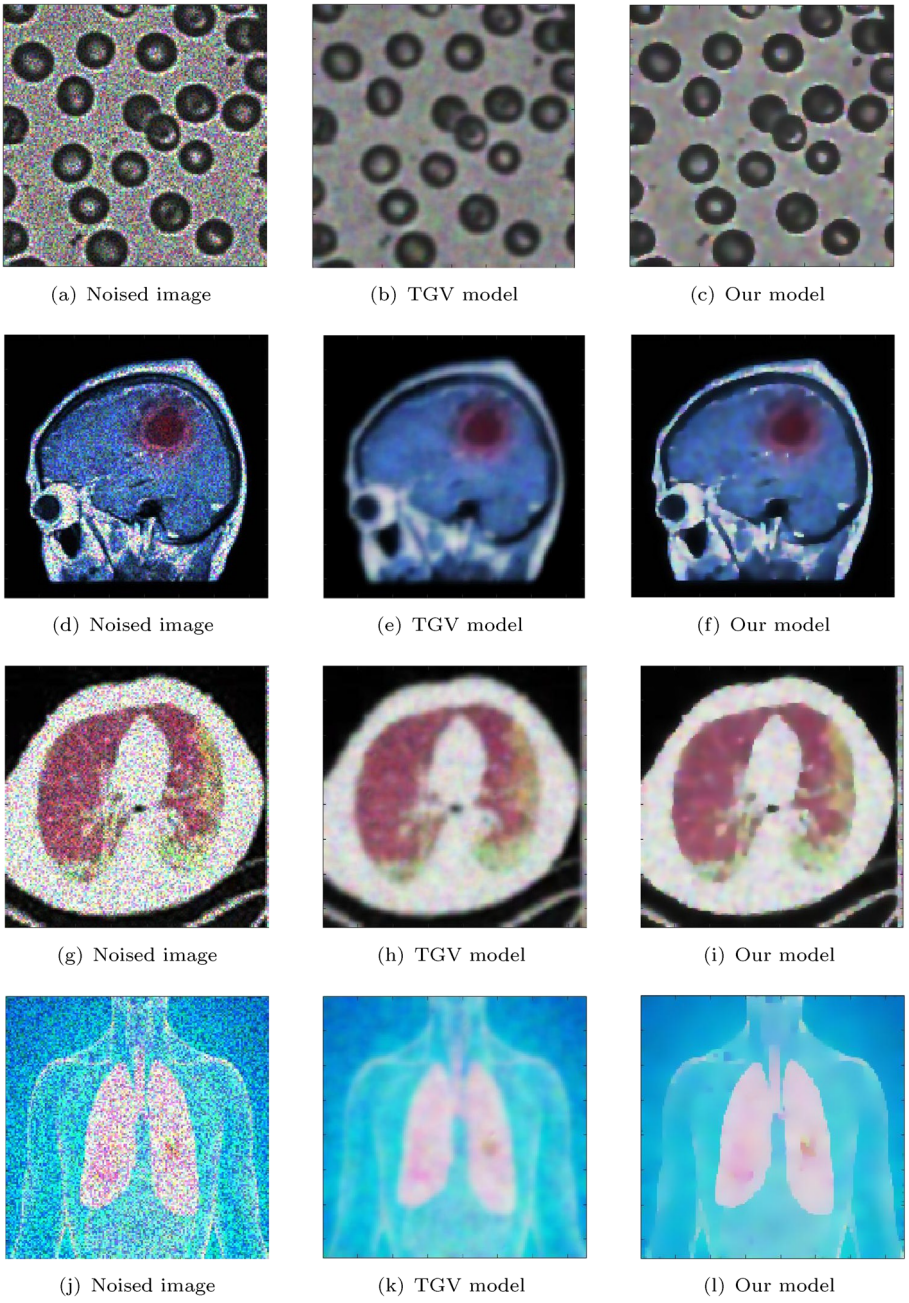

(a) Noised image (b) TGV model (c) Our model

(d) Noised image (e) TGV model (f) Our model

(g) Noised image (h) TGV model (i) Our model

(j) Noised image (k) TGV model (l) Our model

Fig. 11 Comparison of the restored images obtained by our and TGV model with $\sigma^2 = 0.1$

Table 7 Table for comparaison of results presented in Fig. 10

Image	Indicators	Noisy image	TGV model	Our proposed model
Blood	SSIM	0.562	0.73	0.83
	PSNR	20.37	23.09	27.7
	SNR	13.98	16.7	21.39
Brain color	SSIM	0.76	0.8	0.9
	PSNR	23	21.15	26.6
	SNR	14.62	15	18.5
X-ray horizontal cut	SSIM	0.5455	0.80	0.85
	PSNR	19.23	22.15	24.93
	SNR	15.85	18.74	22.55
Lung cancer	SSIM	0.3124	0.94	0.957
	PSNR	18.8	22.52	24.57
	SNR	15.9	22.17	22.19

Table 8 Table for comparaison of results presented in Figure 11

Image	Indicators	Noisy image	TGV model	Our proposed model
Blood	SSIM	0.43	0.69	0.75
	PSNR	16	22.48	25.1
	SNR	10	16	18.72
Brain color	SSIM	0.68	0.74	0.875
	PSNR	19.41	20	24.15
	SNR	10.9	13.65	16
X-ray horizontal cut	SSIM	0.438	0.76	0.8
	PSNR	15.48	19.7	21.4
	SNR	12	16.34	17.97
Lung cancer	SSIM	0.24	0.9	0.928
	PSNR	15	17.93	21
	SNR	12	17.58	18.6

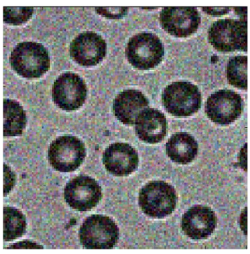

(a) Gaussian noised image (SSIM=0.56 and PSNR=20.17 db)

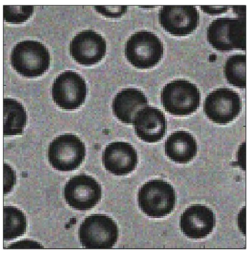

(b) Poisson noised image (SSIM=0.79 and PSNR=27.59 db)

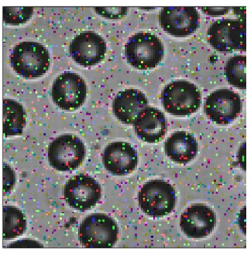

(c) Salt pepper noised image (SSIM=0.57 and PSNR=18.52 db)

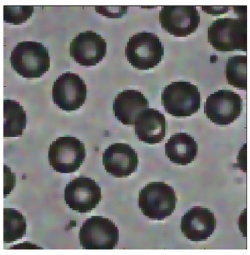

(d) Gaussian restored image (SSIM=0.84 and PSNR= 27 db)

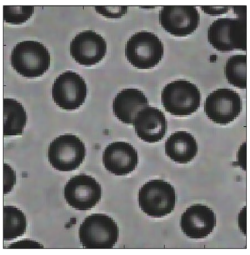

(e) Poisson restored image (SSIM=0.92 and PSNR=31.3 db)

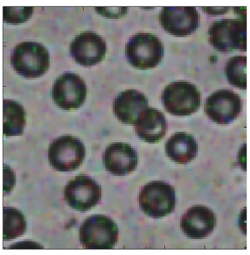

(f) Salt pepper restored image (SSIM=0.77 and PSNR=24 db)

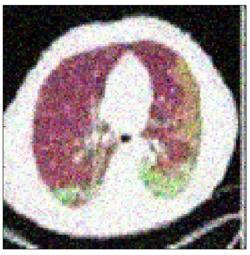

(g) Gaussian noised image (SSIM=0.54 and PSNR=21.32 db)

(h) Poisson noised image (SSIM=0.8 and PSNR=30 db)

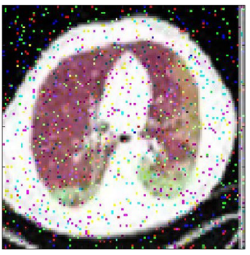

(i) Salt pepper noised image (SSIM=0.548 and PSNR=17.17 db)

(j) Gaussian restored image (SSIM=0.85 and PSNR=26.81 db)

(k) Poisson restored image (SSIM=0.94 and PSNR=31.67 db)

(l) Salt pepper restored image (SSIM=0.75 and PSNR=23.85 db)

Fig. 12 From left to right: removal of Gaussian noise, Poisson noise, and salt and pepper noise by our approach

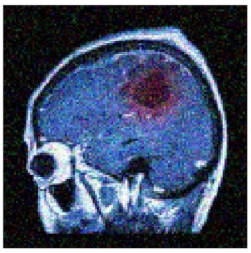

(a) Gaussian noised image (SSIM=0.45 and PSNR=21.26 db)

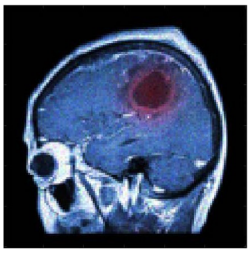

(b) Poisson noised image (SSIM=0.88 and PSNR=30 db)

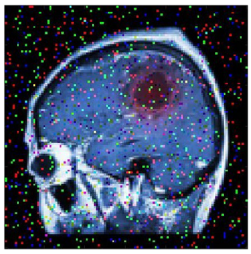

(c) Salt pepper noised image (SSIM=0.49 and PSNR=17 db)

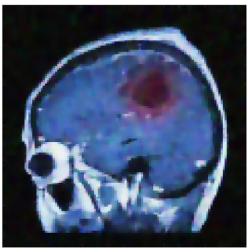

(d) Gaussian restored image (SSIM=0.7 and PSNR= 25.5 db)

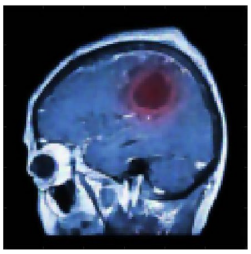

(e) Poisson restored image (SSIM=0.94 and PSNR=31.5 db)

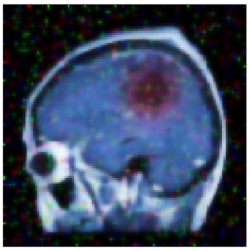

(f) Salt pepper restored image (SSIM=0.65 and PSNR=22.27 db)

(g) Gaussian noised image (SSIM=0.326 and PSNR=21.28 db)

(h) Poisson noised image (SSIM=0.58 and PSNR=27.21 db)

(i) Salt pepper noised image (SSIM=0.367 and PSNR=17 db)

(j) Gaussian restored image (SSIM=0.89 and PSNR=26.5 db)

(k) Poisson restored image (SSIM=0.98 and PSNR=92.35 db)

(l) Salt pepper restored image (SSIM=0.74 and PSNR=24.74 db)

Fig. 13 From left to right: removal of Gaussian noise, Poisson noise, and salt and pepper noise by our approach

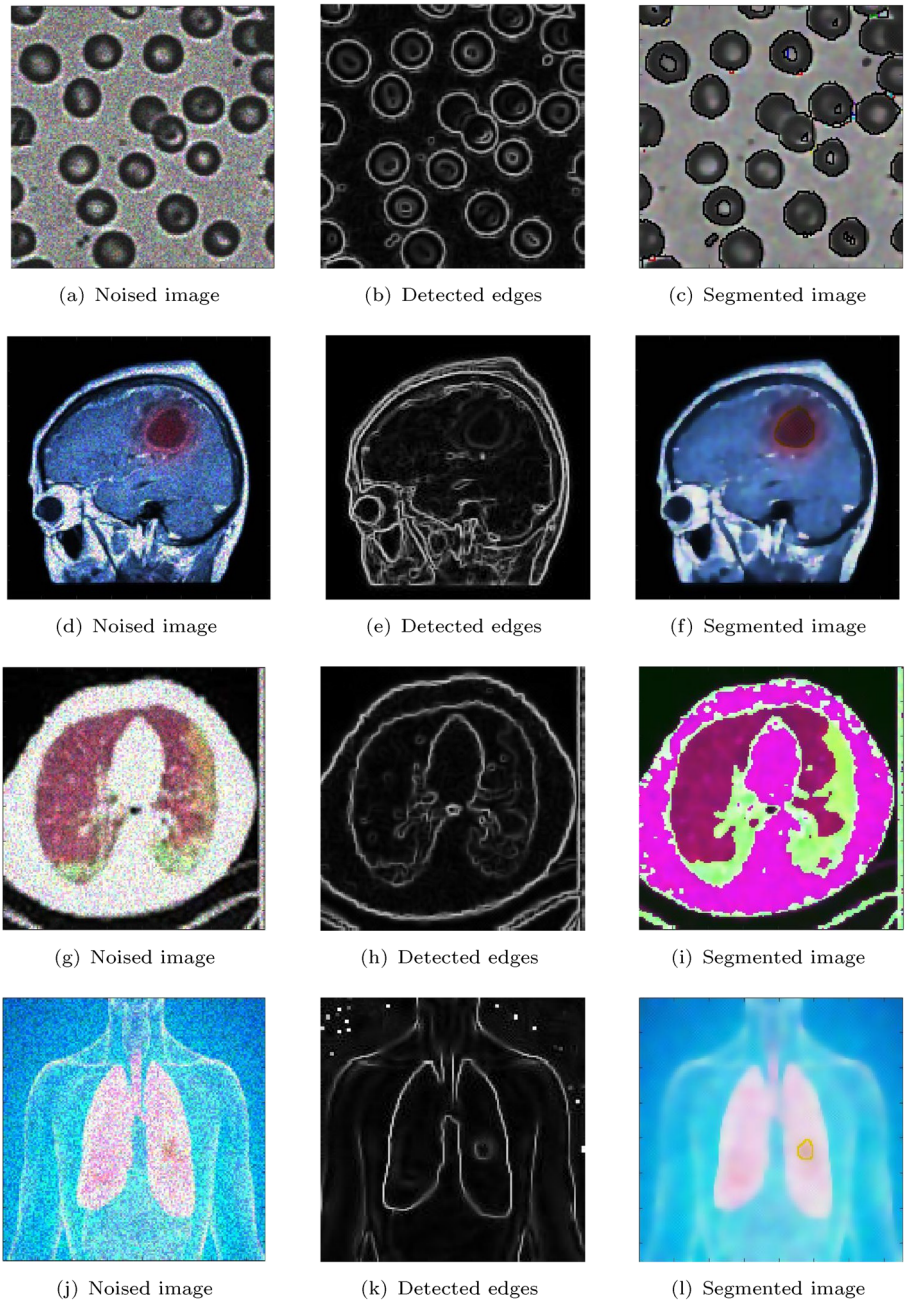

(a) Noised image (b) Detected edges (c) Segmented image

(d) Noised image (e) Detected edges (f) Segmented image

(g) Noised image (h) Detected edges (i) Segmented image

(j) Noised image (k) Detected edges (l) Segmented image

Fig. 14 From left to right: noised image ($\sigma^2 = 0.04$), edges detection by our approach, segmented areas of interest

Data Availability No new data were created or analysed during this study. Data sharing is not applicable to this article.

Declarations

Conflict of interest The authors declare that they have no known competing financial interests or personal relationships that could have appeared to influence the work reported in this paper.

References

1. Ambrosio, G.L., Tortorelli, V.: Approximation of functionals depensing on jumps by elliptic functionals via γ-convergence. Comm. Pure Appl. Math. **43**, 999–1036 (1990)
2. Blomgren, P., Chan, T.: Total variation methods for restoration of vector-valued images. IEEE Trans. Image Process. **7**, 304–309 (1998)
3. Chan, T., Kang, S.H., Shen, J.: Total variation denoising and enhancement of color images based on the CB and HSV color models. J. Vis. Commun. Image Rep. **12**(4), 422–435 (2001)
4. Sapiro, G., Ringach, P.L.: Anisotropic diffusion of multivalued images with applications to color filtering. IEEE Trans. Image Process. **5**, 1582–1585 (1996)
5. Tang, B., Sapiro, G., Caselles, V.: Color image enhancement via chromaticity diffusion. IEEE Trans. Image Process. **10**, 701–707 (2001)
6. Tschumperlé, D.: PDEs based regularization of multivalued images and applications. PhD thesis, Univ. Nice Sophia Antipolis, France (2002)
7. Tschumperlé, D., Deriche, R.: Diffusion PDEs on vector-valued images local approach and geometric viewpoint. IEEE Signal Proces. Mag. **19**, 16–25 (2002)
8. Di Zenzo, S.: A note on the gradient of a multi-image. Comput. Vis. Graph. Image Process. **33**, 116–125 (1986)
9. Jin, Z., Yang, X.: A variational model to remove the multiplicative noise in ultrasound images. J. Math. Imag. Vis. **39**(1), 62–74 (2011)
10. Krissian, K., Kikinis, R., Westin, C.F., Vosburgh, K.: Speckle constrained filtering of ultrasound images. IEEE Conf. Comput. Vis. Pattern. Recognit. **2**, 547–552 (2005)
11. Loupas, T.: Digital image processing for noise reduction in medical ultrasonics. PhD thesis, Univ. Edinburgh, UK (1988)
12. Gonzalez, R., Wood, R.: Digital Image Processing, 3rd edn. Prentice-Hall, Upper Saddle River (2008)
13. Davies, E.R., Charles, D.: Colour image processing: problems, progress and perspectives. In: Marshall, S., Sicuranza, G.L. (eds.) Advances on Nonlinear Signal and Image Processing, pp. 299–325. Hindawi, New York (2006)
14. Koschan, A., Abidi, M.: Digital Color Image Processing. Wiley, Hoboken (2008)
15. Astole, J., Haavisto, P., Neuro, Y.: Vector median filters. In: Proc. IEEE **78**(4), 678–689 (1990)
16. Karakos, D.G., Trahanias, P.E.: Combining vector median and vector directional filters: the directional distance filters. Proc. IEEE Int. Conf. Image Proc. **1**, 171–174 (1995)
17. Trahanias, P.E., Venetsanopoulos, A.N.: Vector directional filters - a new class of multichannel image processing filter. IEEE Trans. Image Process. **2**(4), 528–534 (1993)
18. Brook, A., Kimmel, R., Sochen, N.: Variational restoration and edge detection for color images. J. Math. Imag. Vis. **18**, 247–268 (2003)
19. Kimmel, R., Malladi, R., Sochen, N.: Image processing via the Beltrami operator. In: Proc. Third Asian Conf. Computer Vision., pp. 574–581 (1998)
20. Auroux, D., Belaid, L.J., Rjaibi, B.: Application of the topological gradient method to color image restoration. SIAM J. Imag. Sci. **3**(2), 153–175 (2010)
21. Houichet, H., Theljani, A., Rjaibi, B., Moakher, M.: A nonstandard higher-order variational model to speckle noise removal and thin-structure detection. J. Math. Study **52**(4), 394–424 (2019)
22. Taarabti, S., El Allali, Z., Ben Haddouch, K.: Eigenvalues of the p(x)-biharmonic opeartor with indefinite weight under Neumann boundary conditions. Bol. Socied. Paran. Matem. **36**(1), 195–213 (2018)
23. Houichet, H., Theljani, A., Moakher, M.: A nonlinear fourth-order PDE for image denoising in Sobolev spaces with variable exponents and its numerical algorithm. Comput. Appl. Math. **40**, 70 (2021)
24. Aubert, G., Drogoul, A.: Topological gradient for a fourth order operator used in image analysis. ESAIM: Contr. Optim. Calc. Var. **21**(4), 1120–1149 (2015)
25. Fan, X.L., Zhao, D.: On the spaces $L^{p(x)}(\omega)$ and $W^{m,p(x)}(\omega)$. J. Math. Anal. Appl. **236**, 424–446 (2001)

26. Mihailescu, M.: Existence and multiplicity of solutions for a Neumann problem involving the p(x)-Laplacian operator. Nonlin. Anal. T.M.A. **67**, 1419–1425 (2007)
27. Aubert, G., Aujol, J.-F.: A variational approach to removing multiplicative noise. SIAM J. Appl. Math. **68**(4), 925–946 (2008)
28. Houichet, H., Moakher, M., Rjaibi, B.: Noise removal and edge detection in ultrasound images by the topological gradient method. New Trends Math. Sci. **4**(7), 421–440 (2019)
29. Thomée, V., Wahlbin, L.: On Galerkin methods in semilinear parabolic problems. SIAM J. Numer. Anal. **12**(3), 378–389 (1975)
30. Jin, L., Liu, H., Xu, X., Song, E.: Improved direction estimation for Di Zenzo's multichannel image gradient operator. Pattern Recognit. **45**(12), 4300–4311 (2012)
31. Steger, C.: Extracting curvilinear structure: a differential geometric approach. In: Computer Vision — ECCV '96, pp. 630–641. Springer, Berlin, Heidelberg (1996)
32. Steger, C.: An unbiased detector of curvilinear structures. IEEE Trans. Pattern Anal. Mach. Intell. **20**(2), 113–125 (1998)
33. Singh, A.: Analysis of image noise removal methodologies for high density impulse noise. Int. J. Comput. Sci. Mob. Comput. **3**(6), 659–665 (2014)
34. Kuan, D., Sawchuck, A., Strand, T., Chavel, P.: Adaptative noise smoothing filter for images with signal dependent noise. IEEE Trans. Pattern Anal. Mach. Intell. **7**(2), 165–177 (1985)
35. Frost, V., Stiles, J., Shanmugan, K., Holtzman, P.: A model for radar images and its application to adaptative digital filtering of multiplicative noise. IEEE Trans. Pattern Anal. Mach. Intell. **2**, 157–165 (1982)
36. Florian, K., Kristian, B., Thomas, B., Rudolf, S.: Second order total generalized variation (tgv) for mri. Magn. Resonan. Med. **65**(2), 480–491 (2011)
37. Belaid, L.J., Mourou, W.: Image segmentation: a watershed transformation algorithm. Image Anal Stereol. **28**, 93–102 (2009)